

Hybrid non-uniform recursive subdivision with improved convergence rates

Xin Li^{a,*}, Xiaodong Wei^b, Yongjie Jessica Zhang^b

^a*School of Mathematical Sciences, University of Science and Technology of China, Hefei, Anhui, China*

^b*Department of Mechanical Engineering, Carnegie Mellon University, Pittsburgh, PA 15213, USA*

Abstract

This paper introduces a new non-uniform subdivision surface representation, called hybrid non-uniform subdivision surface (for short, HNUSS). The subdivision scheme is constructed through two steps. The first step inserts a set of edges and converts a valence- n extraordinary point into a valence- n face. The second step combines both primal and dual subdivision schemes to define the subdivision rules. The developed subdivision scheme generalizes bi-cubic NURBS to arbitrary topology and is proved to be G^1 -continuous for any valence extraordinary points and any non-negative knot intervals. The HNUSS limit surface has comparable shape quality as non-uniform subdivision via eigen-polyhedron [1] and has better shape quality than all the other subdivision schemes. In addition, numerical experiments show that HNUSS based isogeometric analysis yields improved convergence rates compared to any existing non-uniform subdivision schemes.

Key words: Non-uniform subdivision, NURBS, Subdivision, Isogeometric analysis

1. Introduction

Isogeometric analysis (IGA) has emerged as a unification technology between computer-aided design (CAD) and numerical simulation. The key insight of IGA is the fact that numerical simulation relies on finite element method with discrete *approximation* of models from CAD, which is classically based on non-uniform rational B-splines (NURBS). The main advantages of the IGA include the elimination of both the geometry approximation error and the computation cost of changing the representation between design and analysis. NURBS are the current standard geometry representation in CAD. NURBS provide intuitive control in the design process, and support fast and stable evaluation. NURBS also offer many advantages in the analysis through IGA [2, 3, 4, 5]. However, a major drawback of NURBS is the tensor-product structure that makes it difficult to model freeform geometry with arbitrary topology. Such a geometry needs to be decomposed into a set of C^{-1} -continuous patches, which often leads to continuity problems during analysis.

There are two main categories of approaches to define representations for extraordinary points (EPs). The first category utilizes a finite number of patches to fill the neighboring region around EPs with many methods developed [6, 7, 8, 9, 10, 11, 12, 13]. Among these methods, manifold splines [13] and smooth cubic splines [14, 15] observe optimal convergence rates. The other category utilizes subdivision with an infinite number of patches around the EPs [16]. Subdivision algorithms are a generalization of splines to define free-form surfaces of arbitrary topology, which is the standard in the animation industry. Subdivision surfaces are also attractive in IGA [17, 18, 19, 20, 21, 22]. Subdivision-based local refinement and its application in IGA have been studied for both Catmull-Clark subdivision [23, 24] and Loop subdivision [25]. However, subdivision schemes are limited to generalizations of uniform splines. In order to make subdivision



*Corresponding author, lixustc@ustc.edu.cn, tel: 86-551-63607202

compatible to NURBS, we need to derive subdivision schemes which can support non-uniform splines. This issue was firstly addressed in [26], and later was extended in [27, 28, 29, 30, 1].

In this paper, we aim to develop a subdivision technique which can support non-uniform splines with arbitrary topology and improved convergence rates. Particularly, this paper focuses on how to define a non-uniform subdivision scheme such that it can be used for both design (shape quality near EPs) and analysis (with improved convergence rates). For this purpose, we present a new *Hybrid Non-Uniform Subdivision Scheme* (for short, HNUSS). The HNUSS is constructed through two steps. The first step converts each EP into an extraordinary face by inserting a set of edges, and then in the second step we define a new subdivision scheme which combines the primal and dual subdivision schemes in the subsequent levels. The main features of the new subdivision scheme include:

1. The HNUSS generalizes bi-cubic NURBS to arbitrary topology;
2. The HNUSS limit surface is proved to be G^1 -continuous for any valence EPs and has satisfactory geometric quality for non-uniform parameterization. To the authors' best knowledge, this is the first paper which can prove G^1 continuity for non-uniform EPs.
3. Numerical experiments show that HNUSS-based IGA yields improved convergence rates compared to all the existing non-uniform subdivision schemes.

The rest of the paper is organized as follows. Section 2 reviews the existing non-uniform subdivision schemes and then we discuss how to construct the new HNUSS in Section 3. Geometric modeling and isogeometric analysis based on HNUSS are discussed in Sections 4 and 5, respectively. The last section draws conclusion and points out future work.

2. Existing non-uniform subdivision schemes

The most popular way to generalize splines to arbitrary topology is using subdivision. This has been well studied for uniform splines [31]. In the non-uniform case, subdivision in regular regions away from EPs is equivalent to NURBS refinement, which relies on the conventional knot insertion: a knot is inserted midway between each pair of existing knots. Referring to the notations in Figure 1, V , E_i and F_i denote the control points at the current level and \bar{V} , \bar{E}_i , \bar{F}_i denote the corresponding control points after subdivision. Then the refinement rule can be summarized as follows. Each face/edge/vertex point is updated using its neighboring vertex points, edge points and face points, for example,

$$\bar{F}_0 = \frac{(d_1 + 2d_0)(e_1 + 2e_0)V + (d_1 + 2d_2)(e_1 + 2e_0)E_0 + (d_1 + 2d_0)(e_1 + 2e_2)E_1 + (d_1 + 2d_2)(e_1 + 2e_2)F_0}{4(d_0 + d_1 + d_2)(e_0 + e_1 + e_2)}, \quad (1)$$

$$\bar{E}_0 = \frac{e_2\bar{F}_0 + e_1\bar{F}_3}{2(e_1 + e_2)} + \frac{M_0}{2}, \quad (2)$$

$$\bar{V} = \frac{e_2\bar{E}_1 + e_1\bar{E}_3}{2(e_1 + e_2)} + \frac{d_2M_0 + d_1M_2}{4(d_1 + d_2)} + \frac{V}{4}, \quad (3)$$

$$\text{where } M_0 = \frac{(d_1 + 2d_0)V + (d_1 + 2d_2)E_0}{2(d_0 + d_1 + d_2)} \text{ and } M_2 = \frac{(d_2 + 2d_3)V + (d_2 + 2d_1)E_2}{2(d_1 + d_2 + d_3)}.$$

There are several different methods to define non-uniform subdivision around EPs, where knot information are coupled with knot intervals by assigning a non-negative number to each edge of the control grid. In [20], the subdivision rule around EPs was formulated by replacing the undefined knot intervals in Equations (1), (2) and (3) by the average of some knot intervals. Another prior art that aims to unify cubic NURBS and Catmull-Clark surfaces into a single representation includes Extended Subdivision Surfaces [27] and Dinus [29]. These schemes handle EPs by reverting to Catmull-Clark rules, and ignoring the actual knot

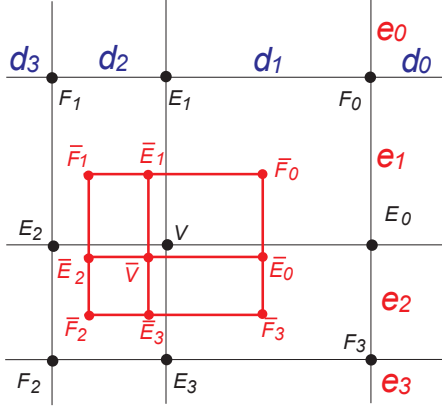


Figure 1: Bi-cubic NURBS can be regarded as the limit of knot splitting process.

intervals. A strategy [28] was proposed to minimize the difference in knot intervals around an EP, which repeatedly splits the largest knot interval at an EP if it is more than twice as large as the smallest knot interval at that EP, and then performs a local refinement to make all knot intervals the same. The refinement rules in [26] was modified by changing the average to the maximal knot interval in [30]. All the above schemes suffer from the same problem of their corresponding limit surfaces: with non-uniform knot intervals, the blending functions of EPs can have two local maxima. This problem has been solved by the technique of eigen-polyhedron [1], where numerical experiments showed that the limit surface is G^1 -continuous at the EPs of valence between 3 and 8. However, it is still an open problem to provide a solid proof for that.

3. Construction of HNUSS

In this section, we discuss how to construct HNUSS in detail. Given a control grid of arbitrary topology with predefined knot intervals, we need to define a blending function for each vertex such that it specializes to NURBS when the valence of each vertex is four. As shown in Figure 2, d_i , \tilde{d}_i , \bar{d}_i , and a_i , \tilde{a}_i , \bar{a}_i are knot intervals and can be any non-negative real numbers. Our discussion assumes that the control grid is a regular manifold grid and all the faces are quadrilaterals. If the assumption does not hold initially, we apply a single NURSS refinement [26, 1] in advance. We assume knot intervals on the opposite edges are the same, i.e., $d_i = \tilde{d}_i = \bar{d}_i$, and $a_i = \tilde{a}_i = \bar{a}_i$.

On a quadrilateral mesh, a regular vertex has a valence of four in the interior, a valence of three on the boundary and a valence of two at the corner. It is called an irregular vertex or extraordinary point otherwise. Topologically a regular vertex in the interior is a crossing of two coordinate lines in a 2D cartesian grid, where we can easily build a right-handed local coordinate system cyclically. A parametric line is generated by tracing a local coordinate direction through regular vertices and ending with extraordinary points or boundary vertices. It is a connected by a sequence of edges, such that two subsequent edges are always connected through a regular vertex where both edges belong to the same local parametric direction. Vertices and edges on the parametric lines are called *virtual vertices* and *virtual edges*, the meaning of which will be clear in the following. As illustrated in Figure 3 (a), all the red edges are virtual edges and all the black and green vertices are virtual vertices. Here red dots represent regular vertices.

The hybrid subdivision contains two steps of rules: a topological step and a geometric step. The topological rules of the first step yield a hybrid dual mesh, as illustrated in Figure 3. At the first level, if a valence- n virtual vertex connects more than two virtual edges, then it is replaced by a dual face consisting

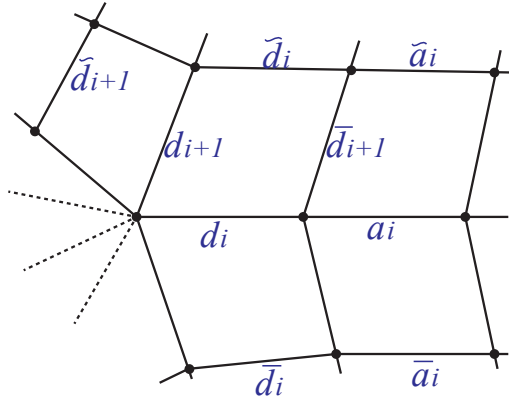


Figure 2: The notations for the initial control grid and knot intervals.

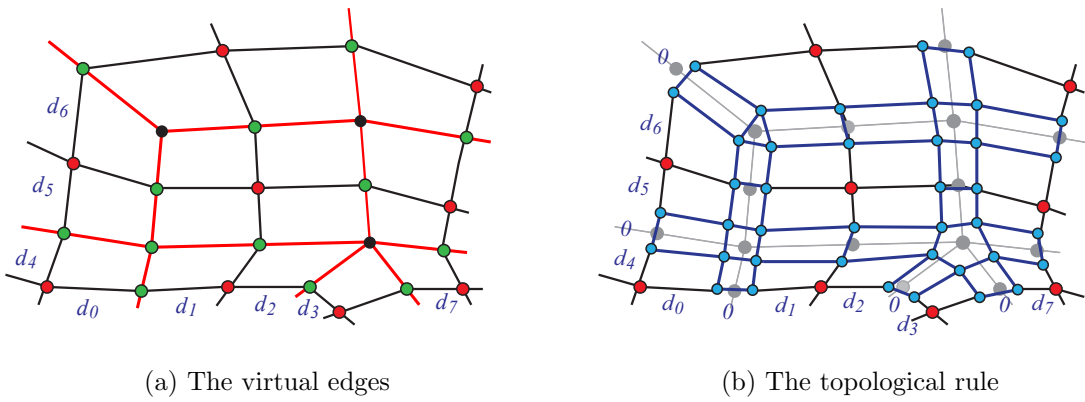


Figure 3: The topological rule of the first level for HNUSS. In (a), the red edges are virtual edges, the black and green vertices are virtual vertices, where two black ones are also EPs. The final mesh after first level subdivision is shown in (b).

of n new vertices, and otherwise it splits into two new vertices. Each virtual edge is then replaced by a dual face. In this manner, we obtain a hybrid dual mesh; see the blue vertices in Figure 3 (b). Edges of each dual face corresponding to an EP are assigned with zero knot intervals and the knot intervals of edges touching non-virtual vertices are kept unchanged. Knot intervals for the other dual edges can be inferred from the opposite edges.

The topological rule for the subsequent levels is based on the hybrid dual mesh of the first level, where there are three different types of faces, referring to Figure 4.

- A face with all zero-knot-interval edges: we will not split it topologically;
- A face with two opposite edges of nonzero knot intervals: we split it into two faces at each level;
- A face with all the four edges of nonzero knot intervals: we split it into four faces at each level;

Now, we focus on the geometric rules based on the notations in Figure 5. For the regular control grid, the geometric rule of the first level corresponds to insertion of zero knot intervals. Thus, we can derive the

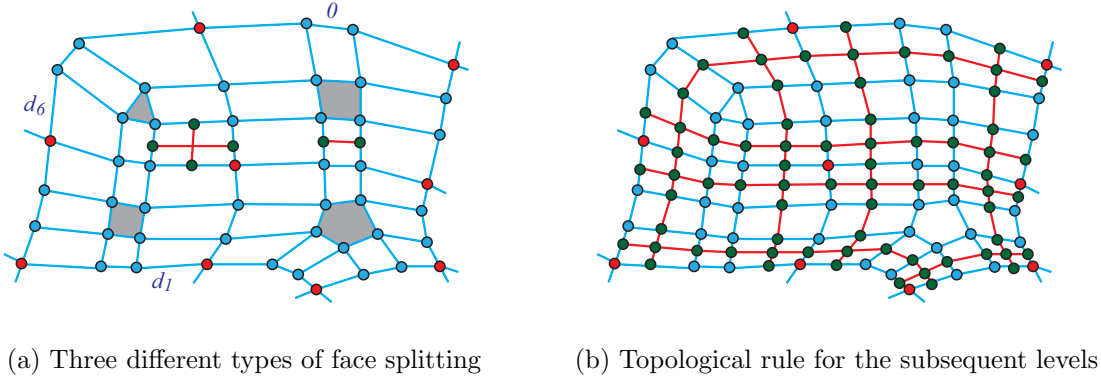


Figure 4: The topological rule of the subsequent levels for HNUSS. (a) shows three different types of face splitting and (b) shows the final mesh after subdivision.

rules directly from non-uniform B-spline knot insertion. Similar to [26], we can derive a heuristic rule for the EPs. Let the grey control grid be the initial control grid and V, E_i, F_i be its vertices. Vertices of the first-level hybrid dual mesh that needs to be updated are calculated as

$$\begin{aligned} P_i^{1,1} &= F_i, \\ P_i^{1,0} &= p_i F_i + (1 - p_i) E_i, \\ P_i^{0,1} &= q_i F_i + (1 - q_i) E_{i+1}, \\ P_i^{0,0} &= p_i q_i F_i + (1 - p_i) q_i E_i + p_i (1 - q_i) E_{i+1} + (1 - p_i) (1 - q_i) V, \end{aligned}$$

where $p_i = \frac{d_{i-1}}{d_{i-1} + d_{i+1} + a_{i+1}}$ and $q_i = \frac{d_{i+2}}{d_{i+2} + d_i + a_i}$. The rule obtained from the above equations is simple but has poor shape quality for non-uniform knot intervals (see Figure 6 as an example). Our construction to define $P_i^{0,0}$ will be discussed in detail in the next section.

The geometric rules for the subsequent levels utilize the notations in Figure 5 (b), where $P_i^{j,k}$ denotes the control points at the current level and $\bar{P}_i^{j,k}$ denotes the corresponding control points after subdivision. We only provide the refinement rules for points $\bar{P}_i^{0,0}, \bar{P}_i^{1,0}, \bar{P}_i^{1,1}$ and $\bar{P}_i^{0,1}$, and the others can be derived from NURBS refinement rules such as Equations (1), (2) and (3). We have

$$\begin{aligned} \bar{P}_i^{1,1} &= \frac{d_i d_{i+1} P_i^{1,1} + d_i (d_{i+1} + 2a_{i+1}) P_i^{1,0} + d_{i+1} (d_i + 2a_i) P_i^{0,1} + (d_i + 2a_i) (d_{i+1} + 2a_{i+1}) P_i^{0,0}}{4(d_i + a_i)(d_{i+1} + a_{i+1})}, \\ \bar{P}_i^{1,0} &= \frac{d_i d_{i+1} P_{i-1}^{0,1} + d_i (d_{i+1} + 2d_{i-1}) P_i^{1,0} + d_{i+1} (d_i + 2a_i) P_{i-1}^{0,0} + (d_i + 2a_i) (d_{i+1} + 2d_{i-1}) P_i^{0,0}}{4(d_{i-1} + d_{i+1})(d_i + a_i)}, \\ \bar{P}_i^{0,1} &= \frac{d_i d_{i+1} P_{i+1}^{1,0} + d_{i+1} (2d_{i+2} + d_i) P_i^{0,1} + d_i (d_{i+1} + 2a_{i+1}) P_{i+1}^{0,0} + (d_{i+1} + 2a_{i+1}) (d_i + 2d_{i+2}) P_i^{0,0}}{4(d_{i-1} + d_{i+1})(d_i + a_i)}, \\ \bar{P}_i^{0,0} &= \frac{P_i^{0,0} + C}{2} + \alpha_i (-n P_i^{0,0} + \sum_{j=0}^{n-1} (1 + 2 \cos(\frac{2(j-i)\pi}{n})) P_j^{0,0}), \end{aligned}$$

$$C = \frac{\sum_{i=0}^{n-1} (d_{i-1} + d_{i+3})(d_i P_{i+1}^{0,0} + d_{i+2} P_i^{0,0})}{\sum_{j=0}^{n-1} (d_j + d_{j+2})(d_{j-1} + d_{j+3})} \doteq \sum_{i=0}^{n-1} \beta_i P_i^{0,0}. \quad (4)$$

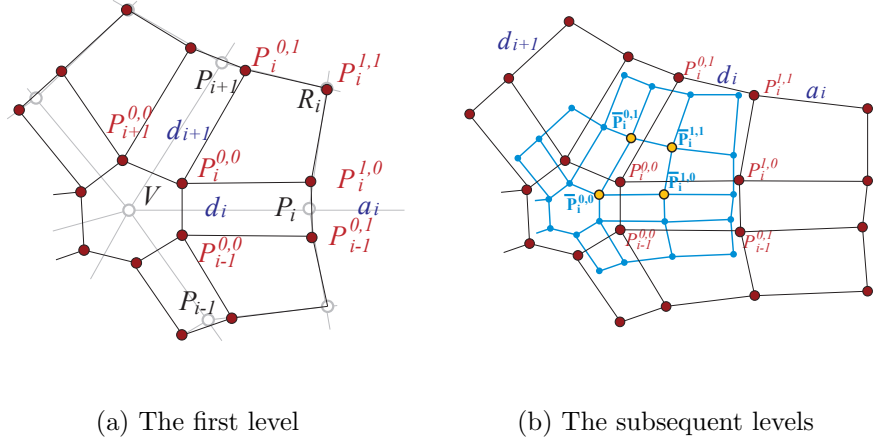


Figure 5: The geometric rules for the HNUSS. (a) is the rule for the first level while (b) is the rule for the subsequent levels.

Remark 1. There are two main differences between the geometric rule for $\bar{P}_i^{0,0}$ and the non-uniform Doo-Sabin subdivision scheme [26]. One is the rule to define α_i : our proposed rule can guarantee that both the second and the third eigenvalues of the subdivision matrix are $\frac{1}{2}$ while the non-uniform Doo-Sabin subdivision scheme can be divergent. The second difference is the rule to define the point C in equation (4) which can be used to prove the characterization map is regular and injective.

Remark 2. The HNUSS can be generalized to the rational representation by assigning a weight for each vertex. The rational control points can be projected into R^4 , subdivided using the same rule, and then projected back into R^3 .

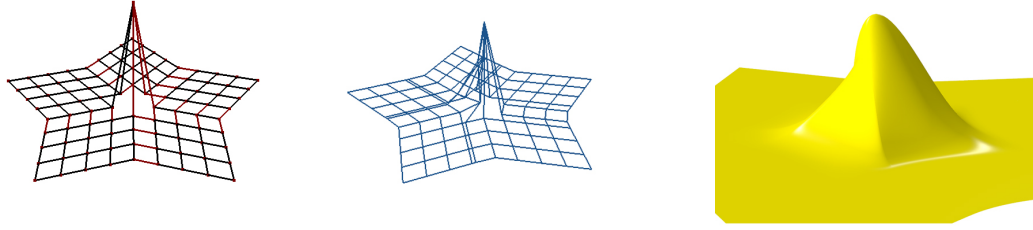
Theorem 1. The HNUSS limit surface is globally G^1 -continuous on 2-manifold control mesh with arbitrary topology and any positive knot intervals.

Proof. This theorem follows directly from Lemma 1 and Lemma 3 according to the subdivision book [32]. Details of their proofs are given in the appendix. \square

4. Geometric modeling with HNUSS

Although the first level of geometric rule does not change the continuity and convergence rates, the geometric rule is very important for the final shape quality; see Figure 6 as an example. The rule derived in Section 3 cannot provide satisfactory shape quality for non-uniform knot intervals. In this section, we provide improved geometric rules for the first level hybrid dual mesh. The basic idea is to use the limit point and tangent plane of the non-uniform subdivision via eigen-polyhedron to guide the construction of these rules.

In this section, we first review the NURSS scheme in [26] and non-uniform subdivision via eigen-polyhedron [1]. Figure 7 shows a valence- n EP V with the neighboring control points E_i and F_i , the knot intervals d_i and a_i , $i = 0, \dots, n-1$. We need to define rules to compute new control points \bar{V} , \bar{E}_i and



(a) The first level grid (b) The second level grid (c) The corresponding limit surface

Figure 6: The blending functions for a valence-5 EP with non-uniform knot intervals using the rule in Section 3 could produce a poor-quality surface even though the surface is G^1 -continuous.

\bar{F}_i . Let $P = [V, E_0, \dots, E_{n-1}, F_0, \dots, F_{n-1}]^T$ and $\bar{P} = [\bar{V}, \bar{E}_0, \dots, \bar{E}_{n-1}, \bar{F}_0, \dots, \bar{F}_{n-1}]^T$, the rules in [26] can be written into a matrix form $\bar{P} = MP$.

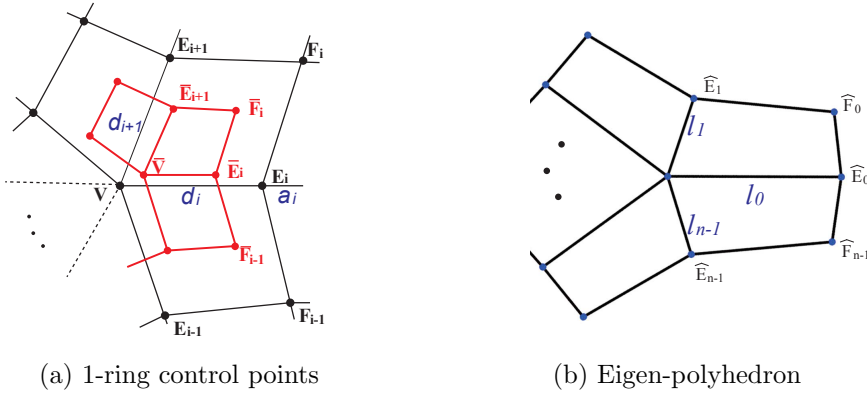


Figure 7: Notations for defining the non-uniform subdivision rule.

- Face points:

$$\bar{F}_i = \omega_i \omega_{i+1} F_i + (1 - \omega_i) \omega_{i+1} E_{i+1} + (1 - \omega_{i+1}) \omega_i E_i + (1 - \omega_i)(1 - \omega_{i+1}) V, \quad (5)$$

where $\omega_i = \frac{d_{i-2} + d_{i+2} + d_i}{d_{i-2} + d_{i+2} + 2d_i + 2a_i}$.

- Edge points:

$$\bar{E}_i = \frac{d_{i-1}}{2(d_{i-1} + d_{i+1})} \bar{F}_i + \frac{d_{i+1}}{2(d_{i-1} + d_{i+1})} \bar{F}_{i-1} + \frac{1}{2} M_i, \quad (6)$$

where $M_i = \omega_i E_i + (1 - \omega_i) V$.

- Vertex Point:

$$\bar{V} = \frac{n-3}{n} V + \frac{3}{n} \frac{\sum_{i=0}^{n-1} (m_i M_i + f_i \bar{F}_i)}{\sum_{i=0}^{n-1} (m_i + f_i)}, \quad (7)$$

The Trial Version where $f_i = d_{i-1} d_{i+2}$, $m_i = f_i + f_{i-1}$.

Instead of defining the rules directly, a polyhedron in R^2 called the eigen-polyhedron is first defined and then the subdivision rules are defined based on the eigen-polyhedron. Referring to Figure 7, denote

$\gamma = \frac{4}{\cos(\frac{2\pi}{n})+1+\sqrt{(\cos(\frac{2\pi}{n})+9)(\cos(\frac{2\pi}{n})+1)}}$ and $\lambda = \frac{1+\gamma}{4\gamma}$. Let $l_i = \frac{2d_i+d_i^-}{3}$, where $d_i^- = \frac{d_{i-2}d_{i+1}+d_{i+2}d_{i-1}}{d_{i-1}+d_{i+1}}$. We define a set of points \widehat{V} , \widehat{E}_i and \widehat{F}_i in R^2 , i.e., $\widehat{V} = (0, 0)$, $\widehat{E}_i = l_i(\cos \frac{2i\pi}{n}, \sin \frac{2i\pi}{n})$ and $\widehat{F}_i = \gamma(\widehat{E}_i + \widehat{E}_{i+1})$. Then the subdivision rules can be defined in the following and the relationship can be written into a matrix form $\overline{P} = NP$.

- Vertex Point: the same as the NURSS rules and let \overline{V} be the point of applying Equation (7) by replacing V , E_i and F_i with \widehat{V} , \widehat{E}_i and \widehat{F}_i , respectively.
- Face points:

$$\overline{F}_i = \alpha_{i,1}\alpha_{i,2}F_i + (1 - \alpha_{i,1})\alpha_{i,2}E_{i+1} + \alpha_{i,1}(1 - \alpha_{i,2})E_i + (1 - \alpha_{i,1})(1 - \alpha_{i,2})V, \quad (8)$$

where $\alpha_{i,1}$ and $\alpha_{i,2}$ are the unique solution of the function

$$\overline{V} + \lambda \widehat{F}_i = \alpha_{i,1}\alpha_{i,2}\widehat{F}_i + (1 - \alpha_{i,1})\alpha_{i,2}\widehat{E}_{i+1} + \alpha_{i,1}(1 - \alpha_{i,2})\widehat{E}_i + (1 - \alpha_{i,1})(1 - \alpha_{i,2})\widehat{V}. \quad (9)$$

- Edge points:

$$\overline{E}_i = (1 - \beta_{i,2})(\frac{1 - \beta_{i,1}}{2}P_{i,1} + \frac{\beta_{i,1}}{2}P_{i,2} + \frac{1}{2}V) + \beta_{i,2}(\frac{1 - \beta_{i,1}}{2}P_{i,3} + \frac{\beta_{i,1}}{2}P_{i,4} + \frac{1}{2}E_i), \quad (10)$$

where

$$P_{i,1} = (1 - \alpha_{i-1,1})V + \alpha_{i-1,1}E_{i-1}, \quad P_{i,2} = (1 - \alpha_{i,2})V + \alpha_{i,2}E_{i+1}; \quad (11)$$

$$P_{i,3} = (1 - \alpha_{i-1,1})E_i + \alpha_{i-1,1}F_{i-1}, \quad P_{i,4} = (1 - \alpha_{i,2})E_i + \alpha_{i,2}F_i, \quad (12)$$

and $\beta_{i,1}$ and $\beta_{i,2}$ are the unique solution of the function

$$\overline{V} + \lambda \widehat{E}_i = (1 - \beta_{i,2})(\frac{1 - \beta_{i,1}}{2}\widehat{P}_{i,1} + \frac{\beta_{i,1}}{2}\widehat{P}_{i,2} + \frac{1}{2}\widehat{V}) + \beta_{i,2}(\frac{1 - \beta_{i,1}}{2}\widehat{P}_{i,3} + \frac{\beta_{i,1}}{2}\widehat{P}_{i,4} + \frac{1}{2}\widehat{E}_i), \quad (13)$$

where $\widehat{P}_{i,j}$ are defined by replacing V , E_i and F_i in Equation (11) with \widehat{V} , \widehat{E}_i and \widehat{F}_i .

4.2. Geometric rule for the first level

Based on the knowledge of eigen-polyhedron, here we provide an improved method to obtain $P_i^{0,0}$. The basic idea is to define $P_i^{0,0}$ as a linear combination of V , E_i and F_i with the guide of the limit point and the tangent plane of the limit surface produced by subdivision via eigen-polyhedron. All the information can be directly computed from the subdivision matrix using Jordan decomposition of matrix N [32].

1. Compute the limit point C for the subdivision scheme based on eigen-polyhedron.

Denote the normalized left eigenvector corresponding to the eigenvalue 1 by $L^0 = [L_0^0, \dots, L_{2n}^0]$ and we have $\sum_{j=0}^{2n} L_j^0 = 1$. The limit point is $C = L^0 M^T P$ according to [32]. Here we also use matrix M because the subdivision scheme based on eigen-polyhedron uses the NURSS rule at the first level.

2. Compute the tangent plane for the subdivision scheme based on eigen-polyhedron.

We define two $2n \times 2n$ matrices \widehat{M} and \widehat{N} , where $\widehat{N}_{i,j} = N_{i+1,j+1} - N_{0,j+1}$, $\widehat{M}_{i,j} = c_i(M_{i+1,j+1} - M_{0,j+1})$, $c_i = \frac{2d_i^-}{2d_i^- + d_i}$, $i = 0, 1, \dots, n-1$ and $c_{i+n} = \frac{c_i + c_{i+1}}{2}$. Let $\widehat{P} = [E_0 - V, \dots, E_{n-1} - V, F_0 - V, \dots, F_{n-1} - V]^T$.

From that according to [1], λ is the leading eigenvalue for the matrix \widehat{N} . \widehat{N} can be written into the form of $\widehat{N} = U\Lambda U^{-1}$, where Λ is a diagonal matrix with the elements being the eigenvalues. Suppose i_1 and i_2 are two indices such that $\Lambda(i_1, i_1) = \Lambda(i_2, i_2) = \lambda$. Let $\widehat{\Lambda}$ be a new diagonal matrix where all the elements are zero except that $\widehat{\Lambda}(i_1, i_1) = \widehat{\Lambda}(i_2, i_2) = 1$. Then we can define a new matrix $Q = U\widehat{\Lambda}U^{-1}$. Now, we can define a set of vectors $\overline{V}_i = [\widehat{M}Q\widehat{P}]_{n+i}$.

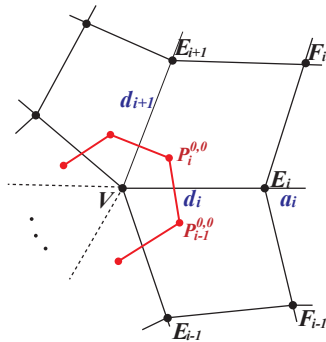


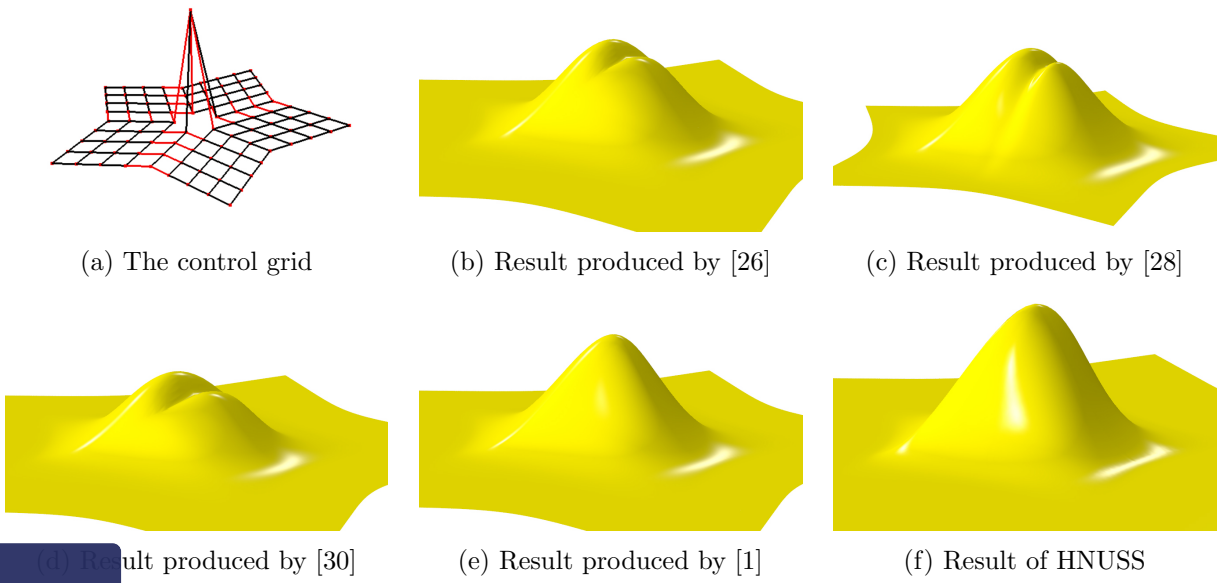
Figure 8: Notations for defining the new HNUSS rule in the first level.

3. Define the subdivision scheme for the EPs at the first level.

Since we have defined the HNUSS for the subsequent levels, the corresponding matrix can define the limit point according to [32]. Denote the limit point C' by applying our new HNUSS subdivision to the control points \bar{V}_i , then

$$P_i^{0,0} = \bar{V}_i + C - C'.$$

Now, we show some HNUSS limit surface examples and compare them with the existing non-uniform subdivision schemes. We first show the graphs of blending functions for the EPs with different valences, such as valence-5 EP in the Figure 9, valence-6 EP in the Figure 10 and valence-7 EP in the Figure 11. We can observe that the HNUSS and the rule in [1] have limit surfaces with similar quality which are much better than the results produced by any other schemes.



The Trial Version

Figure 9: The blending function for a valence-5 non-uniform EP using different approaches, where the knot intervals of the red edges are 10 and those of the other edges are 1.

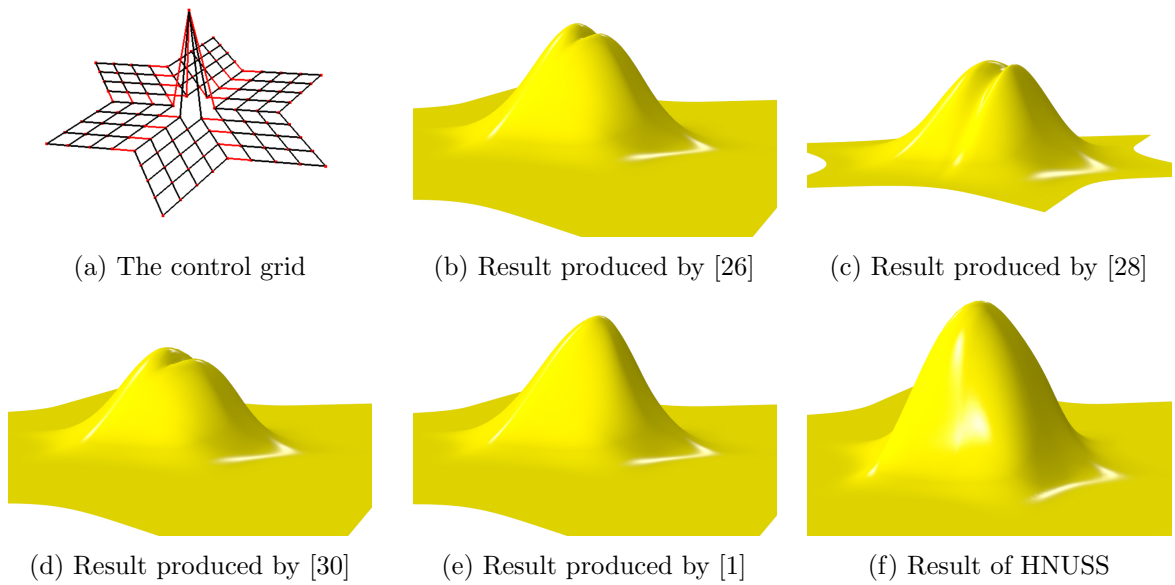


Figure 10: The blending functions for a valence-6 non-uniform EP using different approaches, where the knot intervals of the red edges are 10 and those of the other edges are 1.

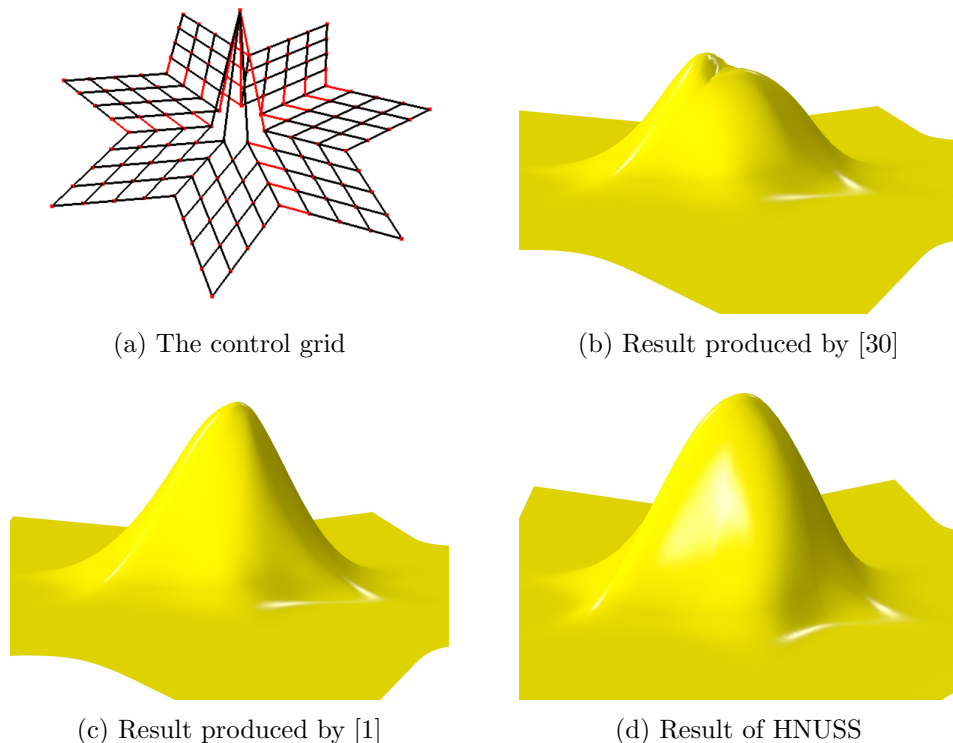


Figure 11: The blending functions for a valence-7 non-uniform EP using different approaches, where the knot intervals for the red edges are 7 and those of the other edges are 1.

The improvement of the blending functions leads to the shape improvement in real-world models, such as the ring model in Figure 12, the helmet model in Figure 13 and Figure 14.

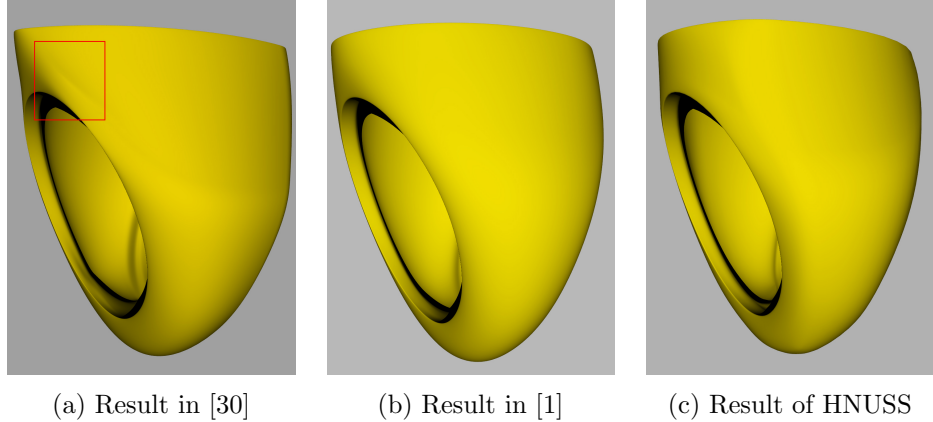


Figure 12: A comparison of three methods ([30], [1] and HNUSS) applied to the ring model. The artifact in the red box of (a) is removed in (b) and (c).

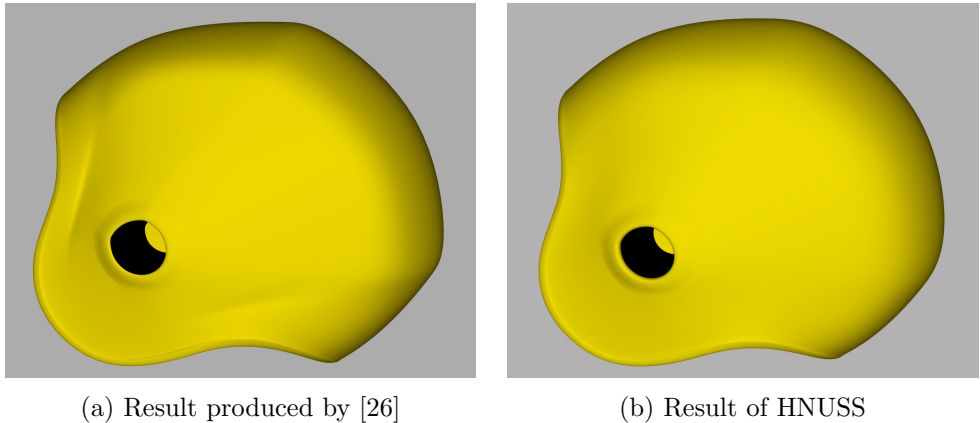


Figure 13: A comparison of two methods ([26] and HNUSS) applied to the helmet model. Some artifacts in (a) are removed in (b).

5. Isogeometric analysis with HNUSS

In this section, we apply the HNUSS to IGA. We first perform a patch test by solving the Poisson's equation on a unit square $[0, 1]^2$ with the following manufactured solution,

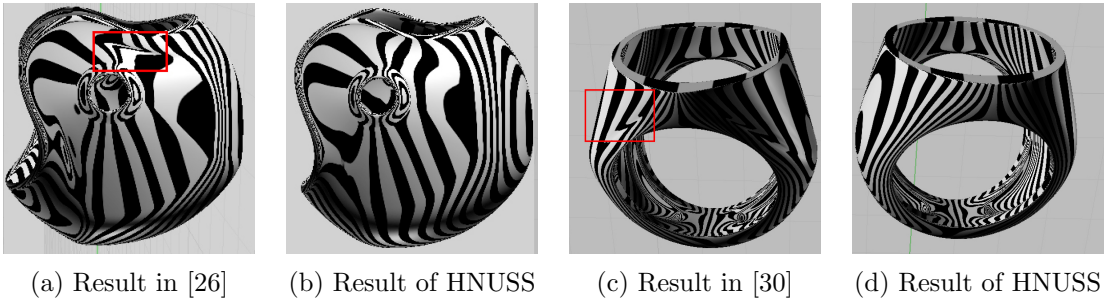


Figure 14: The reflection lines for the helmet and ring models. (a) is the result produced by [26], (c) is the result produced by [30] and (b), (d) are results produced by HNUSS.

several times and adopt 4-point Gaussian quadrature rule for each subelement, which is a common method also used in [12, 24]. The patch test is passed with machine precision with the overall L^2 - and H^1 -norm errors in the order of 10^{-13} and 10^{-11} , respectively; similar results were also observed in [24].

We next numerically test the convergence behavior of the hybrid subdivision. We solve the Poisson's equation on four meshes with EPs of different valence numbers, ranging from 3 to 8; see the input meshes in Figures 15–18. We adopt the following two manufactured solutions,

$$u = \sin(\pi x) \sin(\pi y), \quad (14)$$

and

$$u = e^{(x+y)/2}. \quad (15)$$

L^2 - and H^1 -norm errors are evaluated on six meshes that are obtained through global refinement, which are shown in solid curves in Figures 15–18. The element size is reduced by half in each refinement if measured in the parametric domain, so over refinement we adopt element sizes as 1, 1/2, 1/4, etc. Classical Catmull-Clark subdivision functions [31] are also used to solve the problem for comparison; see dashed curves. We observe that in all the tested meshes, HNUSS possesses faster convergence rates than Catmull-Clark subdivision. Particularly in the high valence cases (valence 6, 7 and 8), HNUSS converges one order faster than Catmull-Clark subdivision. There are also some other papers working on the problem. For example, [22] constructs the subdivision scheme with adapted refinement weights to improve the approximation error, which observes the similar convergence rate as Catmull-Clark subdivision but with small approximation error. We also notice that our results are comparable to those reported in [20], where a dynamic weighted refinement was proposed to make the size of refined irregular elements more uniform than Catmull-Clark subdivision. However, HNUSS can be used in the non-uniform case while the dynamic weighted refinement only supports uniform cases to the authors' best knowledge.

6. Conclusion and future work

This paper has introduced a new non-uniform subdivision scheme called Hybrid Non-Uniform Subdivision Surface or HNUSS.

The subdivision scheme generalizes bi-cubic NURBS to arbitrary topology with satisfactory quality for non-uniform splines with EPs. The subdivision scheme is proved to be G^1 -continuous for any valence EPs with any non-negative knot intervals. HNUSS-based isogeometric analysis has better

convergence rates than the Catmull-Clark subdivision scheme. As the HNUSS representation can be used in both design and analysis, we believe it is a technology with great potential to handle EPs. In the future, we plan to improve HNUSS such that it can achieve optimal convergence rates.

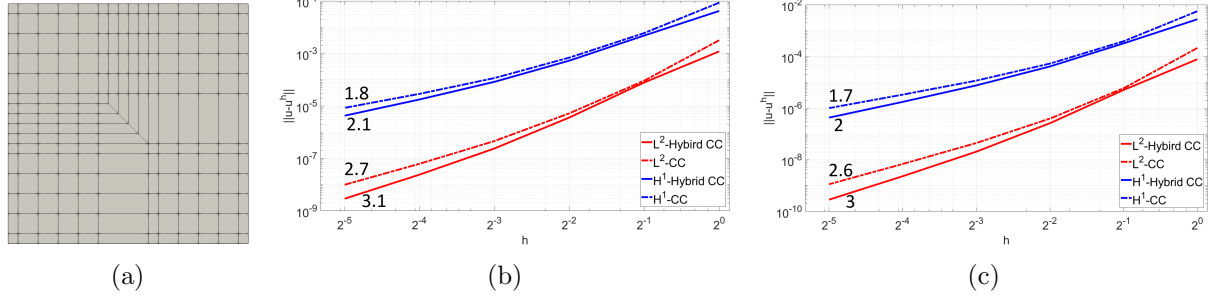


Figure 15: Solving the Poisson's equation on a unit square domain. (a) The input control mesh, and (b, c) convergence curves plotted using the solutions in Equations (14) and (15), respectively.

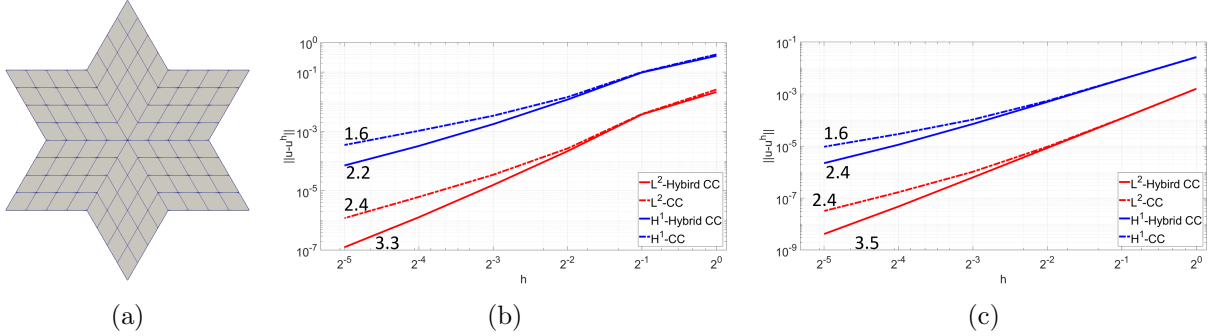


Figure 16: Solving the Poisson's equation on a valence six domain. (a) The input control mesh, and (b, c) convergence curves plotted using the solutions in Equations (14) and (15), respectively.

Acknowledgements

X. Li was supported by the NSF of China (No.61872328), NKBPRPC (2011CB302400), SRF for ROCS SE, and the Youth Innovation Promotion Association CAS. X. Wei and Y. Zhang were supported in part by the PECASE Award N00014-16-1-2254, NSF CAREER Award OCI-1149591 and NSF grant CBET-1804929.

Appendix: proof of the continuity

The new HNUSS surface is always G^1 -continuous for any valence and any non-negative knot intervals. Referring to Figure 19 for the notations, after enough refinement, the hybrid subdivision rule can be written into the following equations.

$$\begin{aligned}
 \bar{P}_j^{0,0} &= \frac{C + P_j^{0,0}}{2} + \alpha_j[-nP_j^{0,0} + \sum_{i=0}^{n-1} (1 + 2 \cos(\frac{2(j-i)\pi}{n}))P_i^{0,0}], \\
 \bar{P}_j^{1,0} &= \frac{6d_{j-1} + 3d_{j+1}}{8(d_{j-1} + d_{j+1})}P_j^{0,0} + \frac{3d_{j+1}}{8(d_{j-1} + d_{j+1})}P_{j-1}^{0,0} + \frac{2d_{j-1} + d_{j+1}}{8(d_{j-1} + d_{j+1})}P_j^{1,0} + \frac{d_{j+1}}{8(d_{j-1} + d_{j+1})}P_{j-1}^{0,1}, \\
 \bar{P}_{j-1}^{0,1} &= \frac{3d_{j-1}}{8(d_{j-1} + d_{j+1})}P_j^{0,0} + \frac{3d_{j-1} + 6d_{j+1}}{8(d_{j-1} + d_{j+1})}P_{j-1}^{0,0} + \frac{d_{j-1}}{8(d_{j-1} + d_{j+1})}P_j^{1,0} + \frac{d_{j-1} + 2d_{j+1}}{8(d_{j-1} + d_{j+1})}P_{j-1}^{0,1}, \\
 \bar{P}_j^{1,1} &= \frac{9}{16}P_j^{0,0} + \frac{3}{16}P_j^{0,0} + \frac{3}{16}P_j^{0,0} + \frac{1}{16}P_j^{1,1}.
 \end{aligned}$$

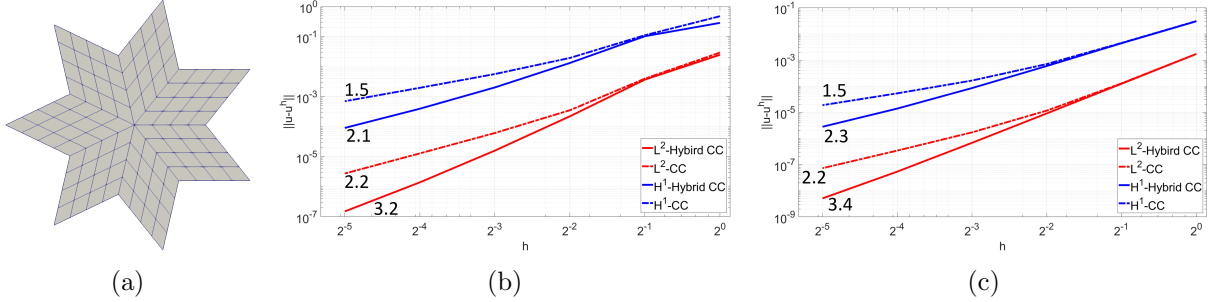


Figure 17: Solving the Poisson's equation on a valence seven domain. (a) The input control mesh, and (b, c) convergence curves plotted using the solutions in Equations (14) and (15), respectively.

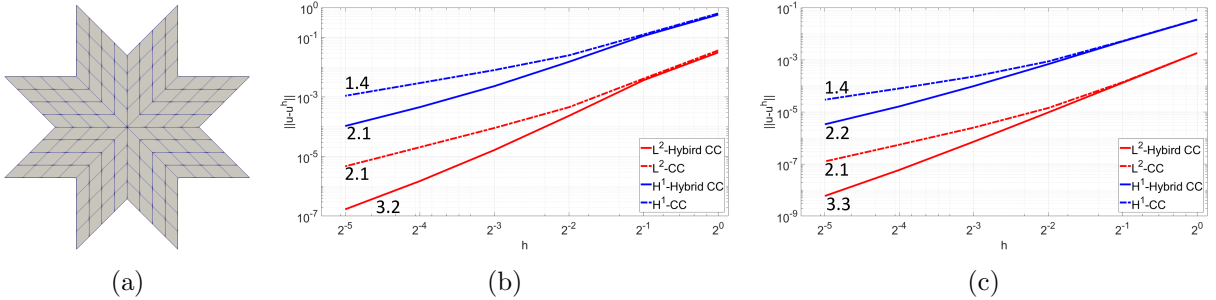


Figure 18: Solving the Poisson's equation on a valence eight domain. (a) The input control mesh, and (b, c) convergence curves plotted using the solutions in Equations (14) and (15), respectively.

The above relation can be written into a matrix form $\bar{P} = S_n P$, and we have

$$\begin{pmatrix} \bar{P}_0^{0,0} \\ \vdots \\ \bar{P}_{n-1}^{0,0} \\ \bar{P}_0^{1,0} \\ \vdots \\ \bar{P}_{n-1}^{0,1} \\ \bar{P}_0^{1,1} \\ \vdots \\ \bar{P}_{n-1}^{1,1} \end{pmatrix} = \begin{pmatrix} Q_n & 0 & 0 \\ T_0 & \dots & 0 \\ \vdots & \ddots & 0 \\ 0 & 0 & T_{n-1} \\ & & \frac{1}{16} & 0 & 0 \\ \ast & \ast & \vdots & \ddots & \\ 0 & 0 & 0 & 0 & \frac{1}{16} \end{pmatrix} \begin{pmatrix} P_0^{0,0} \\ \vdots \\ P_{n-1}^{0,0} \\ P_0^{1,0} \\ \vdots \\ P_{n-1}^{0,1} \\ P_0^{1,1} \\ \vdots \\ P_{n-1}^{1,1} \end{pmatrix}. \quad (16)$$

Denote $Q_n = (Q_{i,j})$, $i, j \in [0, n-1]$, then we obtain

$$Q_{i,j} = \begin{cases} \left(\frac{\beta_j}{2} + (1 + 2 \cos(\frac{2(j-i)\pi}{n}))\alpha_i\right), & j \neq i, \\ \frac{1}{2} + \frac{\beta_i}{2} - (n-3)\alpha_i, & j = i, \end{cases} \quad (17)$$

$$T_j = \begin{pmatrix} \frac{2d_{j-1}+d_{j+1}}{8(d_{j-1}+d_{j+1})} & \frac{d_{j+1}}{8(d_{j-1}+d_{j+1})} \\ \frac{d_{j-1}}{8(d_{j-1}+d_{j+1})} & \frac{d_{j-1}+2d_{j+1}}{8(d_{j-1}+d_{j+1})} \end{pmatrix}. \quad (18)$$

In order to prove the HNUSS is G^1 -continuous, we need to prove that the spectrum of the subdivision

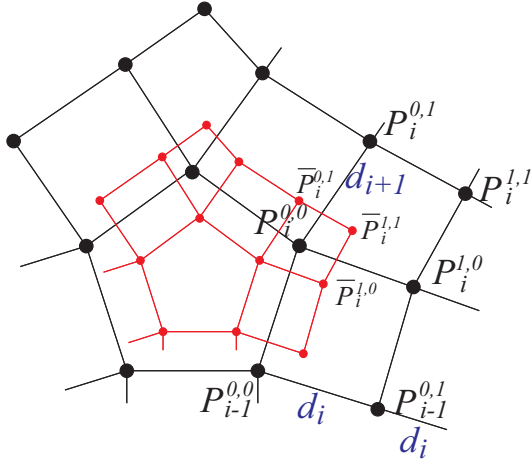


Figure 19: Define the HNUSS subdivision matrix S_n for the 2-ring neighborhood of points around an extraordinary point, where $P_i^{j,k}$ are points before subdivision and $\bar{P}_i^{j,k}$ are points after subdivision.

matrix S_n satisfies some constraints and the associated characterization map is regular and injective. Our proof includes three steps:

1. Prove that the subdivision matrix satisfies the relationship in Lemma 1.
2. Construct the 1-ring neighborhood of control points for the characterization map in Lemma 2;
3. Compute the 4-ring neighborhood of control points for the characterization map and prove that the characterization map is regular and injective in Lemma 3.

Lemma 1. *For any valence EPs, the eigenvalues of the HNUSS subdivision matrix S_n satisfy*

$$\lambda_1 = 1 > \lambda_2 = \lambda_3 = \frac{1}{2} > |\lambda_k|, \quad k = 4, 5, \dots, 4n. \quad (19)$$

Proof. Since the HNUSS subdivision matrix S_n remains constant through all the subsequent subdivision steps, we can use the eigenstructure of S_n to define the characterization map and analyze the continuity. The eigenvalues of S_n consist of those of matrices Q_n , T_i and $\frac{1}{16}I_n$, where Q_n and T_i are defined in Equations (17), and (18) respectively, and I_n is an $n \times n$ identity matrix.

It is obvious that the matrix $\frac{1}{16}I_n$ has n identical eigenvalues $\frac{1}{16}$ and it is easy to verify that the eigenvalues of the 2×2 matrix T_i are $\frac{1}{4}$ and $\frac{1}{8}$. It remains to look into the eigenvalues of Q_n . We use the discrete Fourier transform to analyze the eigenproperties. Let p_k and \bar{p}_k , $(k = 0, \dots, n-1)$ be Fourier vectors corresponding to P_j and \bar{P}_j , i.e.,

$$p_k = \frac{1}{n} \sum_{j=0}^{n-1} P_j^{0,0} \bar{\omega}^{jk}, \quad \bar{p}_k = \frac{1}{n} \sum_{j=0}^{n-1} \bar{P}_j^{0,0} \bar{\omega}^{jk}, \quad (20)$$

$$P_k^{0,0} = \sum_{j=0}^{n-1} p_j \omega^{jk}, \quad \bar{P}_k^{0,0} = \sum_{j=0}^{n-1} \bar{p}_j \omega^{jk}, \quad (21)$$

The Trial Version $\omega = e^{\frac{2\pi}{n}}$ and $\bar{\omega} = e^{-\frac{2\pi}{n}}$. Now the refinement rule can be formulated in terms of the Fourier vectors,

$$\sum_{k=0}^{n-1} \bar{p}_k \omega^{jk} = \sum_{k=0}^{n-1} \left(\sum_{j=0}^{n-1} \frac{\beta_j}{2} \omega^{jk} \right) p_k + p_0 + \frac{\omega^j}{2} p_1 + \frac{\omega^{j(n-1)}}{2} p_{n-1} + \left(\frac{1}{2} - n\alpha_j \right) \sum_{k=2}^{n-2} p_k \omega^{jk}. \quad (22)$$

Using the inverse discrete Fourier transform and we can obtain

$$\begin{pmatrix} \bar{p}_0 \\ \bar{p}_1 \\ \vdots \\ \bar{p}_{n-1} \end{pmatrix} = \begin{pmatrix} 1 & \frac{\beta_1}{2} & \cdots & \frac{\beta_{n-1}}{2} \\ 0 & \frac{1}{2} & \ddots & 0 \\ 0 & 0 & B_{n-3} & 0 \\ 0 & 0 & \ddots & \frac{1}{2} \end{pmatrix} \begin{pmatrix} p_0 \\ p_1 \\ \vdots \\ p_{n-1} \end{pmatrix}, \quad (23)$$

where

$$B_{n-3} = \frac{1}{2}I - \begin{pmatrix} \sum_{j=0}^{n-1} \alpha_j & \sum_{j=0}^{n-1} \alpha_j \omega^j & \cdots & \sum_{j=0}^{n-1} \alpha_j \omega^{(n-4)j} \\ \sum_{j=0}^{n-1} \alpha_j \omega^{(n-1)j} & \sum_{j=0}^{n-1} \alpha_j & \cdots & \sum_{j=0}^{n-1} \alpha_j \omega^{(n-5)j} \\ \vdots & \vdots & \ddots & \vdots \\ \sum_{j=0}^{n-1} \alpha_j \omega^{4j} & \sum_{j=0}^{n-1} \alpha_j \omega^{5j} & \cdots & \sum_{j=0}^{n-1} \alpha_j \end{pmatrix}. \quad (24)$$

However, it is not easy to directly compute the eigenvalue for B_{n-3} . Instead we can construct a circulant matrix G_n as follows:

$$G_n = \begin{pmatrix} \sum_{j=0}^{n-1} \alpha_j & \sum_{j=0}^{n-1} \alpha_j \omega^j & \cdots & \sum_{j=0}^{n-1} \alpha_j \omega^{(n-1)j} \\ \sum_{j=0}^{n-1} \alpha_j \omega^{(n-1)j} & \sum_{j=0}^{n-1} \alpha_j & \cdots & \sum_{j=0}^{n-1} \alpha_j \omega^{(n-2)j} \\ \vdots & \vdots & \ddots & \vdots \\ \sum_{j=0}^{n-1} \alpha_j \omega^j & \sum_{j=0}^{n-1} \alpha_j \omega^{2j} & \cdots & \sum_{j=0}^{n-1} \alpha_j \end{pmatrix}. \quad (25)$$

The eigenvalues μ_k for G_n can be computed explicitly, where $\mu_k = n\alpha_{n-k} \in (0, 1)$, $k = 1, \dots, n$. Denote the eigenvalues for B_{n-3} by $\lambda_{B,i}$, then we can prove that $\lambda_{B,i}$ lies in the domain $(-\frac{1}{2}, \frac{1}{2})$. Actually, G_n is a positive definite matrix, so $\frac{1}{2}I - B_{n-3}$ is also positive definite, which means that $\lambda_{B,i} < \frac{1}{2}$. On the other hand, as $\mu_k < 1$, $I - G_n$ is a positive definite matrix, so $I - (\frac{1}{2}I - B_{n-3})$ is also positive definite, and thus $\lambda_{B,i} > -\frac{1}{2}$. Therefore we can conclude that the eigenvalues of S_n are

$$\lambda_1 = 1 > \lambda_2 = \lambda_3 = \frac{1}{2} > |\lambda_k|, \quad k = 4, 5, \dots, 4n. \quad (26)$$

□

The next step is to compute the characterization map and prove it is regular and injective. We first prove the following lemma.

Lemma 2. Let $P_i = (\cos(\frac{2i\pi}{n}), \sin(\frac{2i\pi}{n})) \in R^2$, $i = 0, \dots, n-1$, $C = \sum_{i=0}^{n-1} \beta_i P_i$, and P be a $n \times 2$ vector containing all the P_i , i.e., $P = [P_0, P_1, \dots, P_{n-1}]^T$, then the HNUSS subdivision matrix S_n satisfies

$$S_n(P - C) = \frac{1}{2}(P - C). \quad (27)$$

Proof. Denote $\bar{P} = S_n P$, then we have

$$\begin{aligned} \bar{P}_j - C &= \frac{P_j - C}{2} + \alpha_j [-n(\cos(\frac{2j\pi}{n}), \sin(\frac{2j\pi}{n})) + \sum_{i=0}^{n-1} (1 + 2\cos(\frac{2(j-i)\pi}{n}))(\cos(\frac{2i\pi}{n}), \sin(\frac{2i\pi}{n}))] \\ &= \frac{P_j - C}{2} + \alpha_j [-n(\cos(\frac{2j\pi}{n}), \sin(\frac{2j\pi}{n})) + \sum_{i=0}^{n-1} 2\cos(\frac{2(j-i)\pi}{n})(\cos(\frac{2i\pi}{n}), \sin(\frac{2i\pi}{n}))] \\ &= \frac{P_j - C}{2} + \alpha_j [-n(\cos(\frac{2j\pi}{n}), \sin(\frac{2j\pi}{n})) + \\ &\quad \sum_{i=0}^{n-1} (\cos(\frac{2j\pi}{n}) + \cos(\frac{2(j-2i)\pi}{n}), \sin(\frac{2j\pi}{n}) - \sin(\frac{2(j-2i)\pi}{n}))] \\ &= \frac{P_j - C}{2}. \end{aligned}$$

The above equation can be applied to any $0 \leq j \leq n - 1$, therefore we can obtain

$$S_n(P - C) = \frac{1}{2}(P - C). \quad (28)$$

□

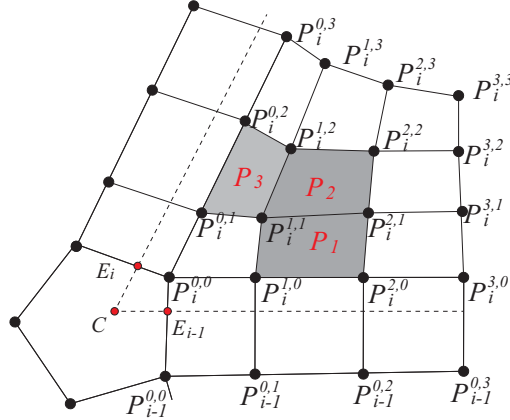


Figure 20: Define the characterization map for HNUSS. The points satisfy $M_n[P_0^{0,0} - C, \dots, P_{n-1}^{0,0} - C]^T = \frac{1}{2}[P_0^{0,0} - C, \dots, P_{n-1}^{0,0} - C]^T$, where M_n is the HNUSS subdivision matrix for the 4-ring neighborhood of points around an extraordinary point.

Lemma 3. *The characterization map for HNUSS is regular and injective for any valence and any positive knot intervals.*

Proof. In order to prove the characterization map is regular and injective, around an EP we need to include 4×4 grid of control points in each segment to prove G^1 continuity. We first need to compute the coordinates of the involved control points, which are used to define the characterization map. The basic idea is based on the fact that applying the subdivision rules to the related control grid is to scale the control grid by half. Referring to Figure 20, let the control grid be $P_i^{j,k}$, $0 \leq j, k \leq 3$, $0 \leq i \leq n - 1$, and the corresponding subdivision matrix be M_n . According to Lemma 2, denote $P_i^{0,0} = P_i = (\cos(\frac{2i\pi}{n}), \sin(\frac{2i\pi}{n})) \in R^2$, $i = 0, \dots, n - 1$, $C = \sum_{i=0}^{n-1} \beta_i P_i$, then $M_n[P_0^{0,0} - C, \dots, P_{n-1}^{0,0} - C]^T = \frac{1}{2}[P_0^{0,0} - C, \dots, P_{n-1}^{0,0} - C]^T$.

Let $E_i = \frac{d_i}{d_i + d_{i+2}} P_{i+1}^{0,0} + \frac{d_{i+2}}{d_i + d_{i+2}} P_i^{0,0}$. For the points $P_{i-1}^{0,1}$ and $P_i^{1,0}$, according to the fact that the new grid after subdivision is the scale of $\frac{1}{2}$ of the given control grid. Using this relationship, we have

$$(1 - \frac{2d_{i-1} + d_{i+1}}{4(d_{i-1} + d_{i+1})})P_i^{1,0} - \frac{d_{i+1}}{4(d_{i-1} + d_{i+1})}P_{i-1}^{0,1} = \frac{6d_{i-1} + 3d_{i+1}}{4(d_{i-1} + d_{i+1})}P_i^{0,0} + \frac{3d_{i+1}}{4(d_{i-1} + d_{i+1})}P_{i-1}^{0,0} - C,$$

$$(1 - \frac{2d_{i+1} + d_{i-1}}{4(d_{i-1} + d_{i+1})})P_{i-1}^{0,1} - \frac{d_{i-1}}{4(d_{i-1} + d_{i+1})}P_i^{1,0} = \frac{3d_{i-1} + 6d_{i+1}}{4(d_{i-1} + d_{i+1})}P_{i-1}^{0,0} + \frac{3d_{i-1}}{4(d_{i-1} + d_{i+1})}P_i^{0,0} - C.$$

Solving the linear systems we get

$$P_i^{1,0} - P_i^{0,0} = P_{i-1}^{0,1} - P_{i-1}^{0,0} = 2(E_{i-1} - C). \quad (29)$$

pdfelement

Similarly, we can compute $P_i^{2,0}$, $P_i^{3,0}$, $P_{i-1}^{0,3}$, $P_{i-1}^{0,3}$ as

$$P_i^{2,0} - P_i^{1,0} = P_{i-1}^{0,2} - P_{i-1}^{0,1} = 3(E_{i-1} - C),$$

$$P_i^{3,0} - P_i^{2,0} = P_{i-1}^{0,3} - P_{i-1}^{0,2} = 3(E_{i-1} - C).$$

Let $p = P_i^{0,0} - C$, $v = E_{i-1} - C$ and $w = E_i - C$, then we compute the remaining control points $P_i^{j,k}$ such that $M_n[P_0^{0,0} - C, P_0^{1,0} - C, \dots, P_{n-1}^{3,3} - C]^T = \frac{1}{2}[P_0^{0,0} - C, P_0^{1,0} - C, \dots, P_{n-1}^{3,3} - C]^T$. We obtain

$$\begin{pmatrix} P_i^{3,1} & P_i^{3,2} & P_i^{3,3} \\ P_i^{2,1} & P_i^{2,2} & P_i^{2,3} \\ P_i^{1,1} & P_i^{1,2} & P_i^{1,3} \end{pmatrix} = C + \begin{pmatrix} \frac{93p+12v+222w}{35} & \frac{939p+393v+1014w}{217} & \frac{5853p+2523v+2523w}{1085} \\ \frac{87p+18v+123w}{35} & \frac{3987p+2523(v+w)}{1085} & \frac{939p+1014v+393w}{217} \\ \frac{15p+6(v+w)}{7} & \frac{87p+123v+18w}{35} & \frac{93p+222v+18w}{35} \end{pmatrix}. \quad (30)$$

With all these control points, we can extract the Bézier control points for the patches P_1 , P_2 and P_3 . For example, the 4×4 Bézier control points for patch P_2 has the explicit form

$$C + \begin{pmatrix} \frac{1901p+1354v+1354w}{1085} & \frac{2221p+2119v+1034w}{1085} & \frac{473p+612v+178w}{217} & \frac{9899p+16141v+3121w}{4340} \\ \frac{2221p+1034v+2119w}{1085} & \frac{535p+333v+333w}{217} & \frac{2901p+2524v+1439w}{1085} & \frac{3074p+3436v+1266w}{1085} \\ \frac{473p+178v+612w}{217} & \frac{2901p+1439v+2524w}{1085} & \frac{3229p+2196v+2196w}{1085} & \frac{3482p+3082v+1943w}{1085} \\ \frac{9899p+3121v+16141w}{4340} & \frac{3074p+1266v+3436w}{1085} & \frac{3482p+1943v+3028w}{1085} & \frac{3802p+2708v+2708w}{1085} \end{pmatrix}.$$

Then two directional derivatives of patch P_2 , $\frac{\partial P_2}{\partial t}$ and $\frac{\partial P_2}{\partial s}$, are bi-degree 3×2 and 2×3 Bézier patches respectively, where vectors of the control points are

$$\frac{\partial P_2}{\partial t} : \begin{pmatrix} \frac{64p-64v+153w}{217} & \frac{454p-454v+631w}{1085} & \frac{536p-536v+549w}{1085} & \frac{2397p-2397v+1943w}{4340} \\ \frac{144p-144v+941w}{1085} & \frac{226p-226v+859w}{1085} & \frac{328p-328v+757w}{1085} & \frac{408p-408v+677w}{1085} \\ \frac{439p-439v+3901w}{4340} & \frac{173p-173v+912w}{1085} & \frac{253p-253v+832w}{1085} & \frac{64p-64v+153w}{217} \end{pmatrix}, \quad (31)$$

$$\frac{\partial P_2}{\partial s} : \begin{pmatrix} \frac{64p+153v-64w}{217} & \frac{144p+941v-144w}{1085} & \frac{439p+3901v-439w}{4340} \\ \frac{454p+631v-454w}{1085} & \frac{226p+859v-226w}{1085} & \frac{173p+912v-173w}{1085} \\ \frac{536p+549v-536w}{1085} & \frac{328p+757v-328w}{1085} & \frac{253p+832v-253w}{1085} \\ \frac{2397p+1943v-2397w}{4340} & \frac{408p+677v-408w}{1085} & \frac{64p+153v-64w}{217} \end{pmatrix}. \quad (32)$$

From Equation (4), we can observe that C is a convex combination of the points E_i , so the control points $P_i^{0,0}$ lie in the regions bounded by two rays CE_{i-1} and CE_i . The control points for $\frac{\partial P_2}{\partial t}$ are convex combinations of vectors p , $-v$ and w , while the control points for $\frac{\partial P_2}{\partial s}$ are convex combinations of vectors p , v and $-w$, so the patch of P_2 is regular and injective. On the other hand, from the above computation, we can observe that for any i , the control points $P_i^{0,0}$, $P_i^{1,0}$, $P_i^{2,0}$ and $P_i^{3,0}$ are also collinear, the control points $P_{i-1}^{0,0}$, $P_{i-1}^{0,1}$, $P_{i-1}^{0,2}$ and $P_{i-1}^{0,3}$ are collinear, and these two lines are parallel. In addition, according to Equation (30), the points $P_i^{j,k}$, $0 \leq j, k \leq 3$, all lie in the regions bounded by two rays CE_{i-1} and CE_i . Thus, the characterization map of HNUSS is regular and injective for any valence and any positive knot intervals. \square

References

- [1] X. Li, T. Finnigin, T. W. Sederberg, G^1 non-uniform Catmull-Clark surfaces, ACM Transactions on Graphics 35 (2016) 1–8.
- [2] T. J. R. Hughes, J. A. Cottrell, Y. Bazilevs, Isogeometric analysis: CAD, finite elements, NURBS, exact geometry, and mesh refinement, Computer Methods in Applied Mechanics and Engineering 194 (2005) 4135–4195.
- [3] J. A. Cottrell, A. Reali, Y. Bazilevs, T. J. R. Hughes, Isogeometric analysis of structural vibrations, Computer Methods in Applied Mechanics and Engineering 195 (2006) 5257–5296.

[4] J. A. Evans, Y. Bazilevs, I. Babuška, T. J. R. Hughes, *n*-Widths, sup-infs, and optimality ratios for the k -version of the isogeometric finite element method, *Computer Methods in Applied Mechanics and Engineering* 198 (21-26) (2009) 1726–1741.

[5] S. Lipton, J. A. Evans, Y. Bazilevs, T. Elguedj, T. J. R. Hughes, Robustness of isogeometric structural discretizations under severe mesh distortion, *Computer Methods in Applied Mechanics and Engineering* 199 (5-8) (2010) 357–373.

[6] T. W. Sederberg, D. L. Cardon, G. T. Finnigan, N. S. North, J. Zheng, T. Lyche, T-spline simplification and local refinement, *ACM Transactions on Graphics* 23 (3) (2004) 276–283.

[7] X. Li, J. Zheng, T. W. Sederberg, T. J. R. Hughes, M. A. Scott, On the linear independence of T-splines blending functions, *Computer Aided Geometric Design*, 29 (2012) 63–76.

[8] J. Zhang, X. Li, On the linear independence and partition of unity of arbitrary degree analysis-suitable T-splines, *Communications in Mathematics and Statistics* 3 (3) (2015) 353–364.

[9] X. Li, J. Zhang, AS++ T-splines: linear independence and approximation, *Computer Methods in Applied Mechanics and Engineering* 333 (2018) 462–474.

[10] J. Zhang, X. Li, Local refinement of analysis-suitable++ T-splines, *Computer Methods in Applied Mechanics and Engineering* 342 (2018) 32–45.

[11] M. A. Scott, R. N. Simpson, J. A. Evans, S. Lipton, S. P. A. Bordas, T. J. R. Hughes, T. W. Sederberg, Isogeometric boundary element analysis using unstructured T-splines, *Computer Methods in Applied Mechanics and Engineering* 254 (2013) 197–221.

[12] T. Nguyen, K. Karčiauskas, J. Peters, A comparative study of several classical, discrete differential and isogeometric methods for solving Poisson's equation on the disk, *Axioms* 3 (2014) 280–300.

[13] M. Majeed, F. Cirak, Isogeometric analysis using manifold-based smooth basis functions, *Computer Methods in Applied Mechanics and Engineering* 326 (2017) 547–567.

[14] D. Toshniwal, H. Speleers, T. Hughes, Smooth cubic spline spaces on unstructured quadrilateral meshes with particular emphasis on extraordinary points: geometric design and isogeometric analysis considerations, *Computer Methods in Applied Mechanics and Engineering* 327 (2017) 411–458.

[15] X. Wei, Y. J. Zhang, D. Toshniwal, H. Speleers, X. Li, C. Manni, J. A. Evans, T. J. Hughes, Blended B-spline construction on unstructured quadrilateral and hexahedral meshes with optimal convergence rates in isogeometric analysis, *Computer Methods in Applied Mechanics and Engineering* 341 (2018) 608–639.

[16] J. Warren, H. Weimer, *Subdivision Methods for Geometric Design*, Morgan Kaufmann, 2002.

[17] F. Cirak, M. Ortiz, P. Schröder, Subdivision surfaces: a new paradigm for thin shell analysis, *International Journal of Numerical Methods in Engineering* 47 (2000) 2039–2072.

[18] D. Burckhart, B. Hamann, G. Umlauf, Iso-geometric finite element analysis based on Catmull-Clark subdivision solids, *Computer Graphics Forum* 29(5) (2010) 1575–1584.

[19] E. Dikici, S. R. Snare, F. Orderud, Isoparametric finite element analysis for Doo-Sabin subdivision models, in: *Proceedings of Graphics Interface*, 2012, pp. 19–26.

- [20] X. Yuan, K. Tang, Rectified unstructured T-splines with dynamic weighted refinement for improvement in geometric consistency and approximation convergence, *Computer Methods in Applied Mechanics and Engineering* 316 (2017) 373–399.
- [21] A. Riffnaller-Schiefer, U. Augsdorfer, D. Fellner, Isogeometric shell analysis with NURBS compatible subdivision surfaces, *Applied Mathematics and Computation* 272 (2016) 139–147.
- [22] Q. Zhang, M. Sabin, F. Cirak, Subdivision surfaces with isogeometric analysis adapted refinement weights, *Computer-Aided Design* 102 (2018) 104–114.
- [23] X. Wei, Y. Zhang, T. J. Hughes, M. A. Scott, Truncated hierarchical Catmull-Clark subdivision with local refinement, *Computer Methods in Applied Mechanics and Engineering* 291 (2015) 1–20.
- [24] X. Wei, Y. Zhang, T. J. R. Hughes, M. A. Scott, Extended truncated hierarchical Catmull-Clark subdivision, *Computer Methods in Applied Mechanics and Engineering* 299 (2016) 316–336.
- [25] H. Kang, X. Li, J. Deng, F. Chen, Truncated hierarchical Loop subdivision surfaces and application in isogeometric analysis, *Computers and Mathematics with Applications* 72 (2016) 2041–2055.
- [26] T. Sederberg, J. Zheng, D. Sewell, M. Sabin, Non-uniform recursive subdivision surfaces, in: *SIGGRAPH '98*, 1998, pp. 387–394.
- [27] K. Muller, L. Reusche, D. Fellner, Extended subdivision surfaces: building a bridge between NURBS and Catmull-Clark surfaces, *ACM Transactions on Graphics* 25 (2006) 268–292.
- [28] T. J. Cashman, U. H. Augsdörfer, N. A. Dodgson, M. A. Sabin, NURBS with extraordinary points: high-degree, non-uniform, rational subdivision schemes, *ACM Transactions on Graphics* 28 (3) (2009) 1–9.
- [29] K. Muller, C. Funzig, L. Reusche, D. Hansford, G. Farin, H. Hagen, DINUS-double insertion, non-uniform, stationary subdivision surfaces, *ACM Transactions on Graphics* 29 (2010) 1–21.
- [30] D. Kovacs, J. Bisceglia, D. Zorin, Dyadic T-mesh subdivision, *ACM Transactions on Graphics* 34 (4) (2015) 143.
- [31] J. Stam, Exact evaluation of Catmull-Clark subdivision surfaces at arbitrary parameter values, *Proceedings of the 25th Annual Conference on Computer Graphics and Interactive Techniques* (1998) 395–404.
- [32] J. Peters, U. Reif, *Subdivision Methods for Geometric Design*, Morgan Kaufmann, 2008.